

A hot Jupiter spectral sequence with evidence for compositional diversity

Megan Mansfield (✉ meganmansfield@uchicago.edu)

University of Chicago <https://orcid.org/0000-0003-4241-7413>

Michael Line

Arizona State University

Jacob Bean

University of Chicago

Jonathan Fortney

University of California, Santa Cruz

Vivien Parmentier

University of Oxford

Eliza Kempton

University of Maryland <https://orcid.org/0000-0002-1337-9051>

David Sing

Johns Hopkins University <https://orcid.org/0000-0001-6050-7645>

Mercedes Lopez-Morales

Harvard University

Claire Baxter

University of Amsterdam

Jean-Michel Désert

University of Amsterdam

Mark Swain

Jet Propulsion Laboratory

Gael Roudier

NASA Jet Propulsion Laboratory

Research Article

Keywords: hot Jupiters, thermal emission spectra, spectral sequence, compositional diversity

Posted Date: October 26th, 2020

DOI: <https://doi.org/10.21203/rs.3.rs-93825/v1>

License:  This work is licensed under a Creative Commons Attribution 4.0 International License.

[Read Full License](#)

Version of Record: A version of this preprint was published at Nature Astronomy on October 21st, 2021.

See the published version at <https://doi.org/10.1038/s41550-021-01455-4>.

A hot Jupiter spectral sequence with evidence for compositional diversity

Megan Mansfield^{1,*}, Michael R. Line², Jacob L. Bean³, Jonathan J. Fortney⁴, Vivien Parmentier⁵, Eliza M.-R. Kempton⁶, David K. Sing⁷, Mercedes López-Morales⁸, Claire Baxter⁹, Jean-Michel Désert⁹, Mark R. Swain¹⁰, and Gael M. Roudier¹⁰

¹Department of Geophysical Sciences, University of Chicago, 5734 S. Ellis Avenue, Chicago, IL 60637, USA

²School of Earth and Space Exploration, Arizona State University, Tempe, AZ 85281, USA

³Department of Astronomy & Astrophysics, University of Chicago, Chicago, IL 60637, USA

⁴Department of Astronomy and Astrophysics, University of California, Santa Cruz, CA 95064, USA

⁵Department of Physics, University of Oxford, Oxford, OX1 3PU, UK

⁶Department of Astronomy, University of Maryland, College Park, MD 20742, USA

⁷Department of Physics & Astronomy, Johns Hopkins University, Baltimore, MD 21218, USA

⁸Center for Astrophysics | Harvard & Smithsonian, Cambridge, MA 01238, USA

⁹Anton Pannekoek Institute for Astronomy, University of Amsterdam, 1098 XH Amsterdam, The Netherlands

¹⁰NASA Jet Propulsion Laboratory, California Institute of Technology, Pasadena, CA 91109, USA

*Corresponding author: meganmansfield@uchicago.edu

ABSTRACT

The emergent spectra of close-in, giant exoplanets (“hot Jupiters”) are believed to be distinct from those of young gas giants and brown dwarfs with similar effective temperatures because these objects are primarily heated from above by their host stars rather than internally from the release of energy from their formation¹. Theoretical models predict a continuum of dayside spectra for hot Jupiters as a function of irradiation level, with the coolest planets having absorption features in their spectra, intermediate-temperature planets having emission features due to thermal inversions, and the hottest planets having blackbody-like spectra due to molecular dissociation and continuum opacity from the H⁻ ion^{2–4}. Absorption and emission features have been detected in the spectra of a number of individual hot Jupiters^{5,6}, and population-level trends have been observed in photometric measurements^{7–11}. However, there has been no unified, population-level study of the thermal emission spectra of hot Jupiters such as has been done for brown dwarfs¹² and transmission spectra of hot Jupiters¹³. Here we show that hot Jupiter secondary eclipse spectra centered around a water absorption band at 1.4 μm follow a common trend in water feature strength with temperature. The observed trend is broadly consistent with the predictions of self-consistent one-dimensional models for how the thermal structures of solar composition planets vary with irradiation level. Nevertheless, the ensemble of planets exhibits significant scatter around the mean trend. The spread can be accounted for if the planets have modest variations in metallicity and/or elemental abundance ratios, which is expected from planet formation models^{14–17}.

We performed a statistical analysis of 14 hot Jupiter secondary eclipse spectra obtained with the Wide Field Camera 3 (WFC3) instrument on the *Hubble Space Telescope* (*HST*) using the G141 grism between 1.1 and 1.7 μm . This bandpass is primarily sensitive to water vapor in exoplanet atmospheres, and the largest molecular feature in this wavelength range is a water vapor absorption band centered at about 1.4 μm . Over the last decade a large sample of exoplanets have been observed using WFC3+G141 to understand their atmospheric water abundances^{13,18}, and it has become an important tool in understanding exoplanet atmospheres.

We analyzed six new data sets following the data reduction procedure outlined in the Methods. We combined these six new analyses with eight results from the literature to form a complete sample of planets observed with *HST*/WFC3+G141 in spatial scanning mode in this wavelength region. Supplementary Table 1 contains detailed information on each of the eight literature results we considered. We limited this study to observations made in the spatial scanning mode and excluded stare mode observations because previous work has shown that instrument systematics are better understood in scanning mode, so the data derived from scanning mode observations are less likely to be complicated by inaccurately corrected systematics¹⁹. The planets in this study have observed dayside temperatures in the *HST*/WFC3+G141 bandpass between 1450 – 3100 K and radii between 0.9 – 2.0 Jupiter radii. The full set of 14 spectra are shown in Figure 1.

Baxter et al. (2020)⁹ presented an analysis of changes in the thermal emission spectra of a subset of planets observed with *HST*. This study expands on that work by uniformly an-

49 analyzing all *HST* thermal emission spectra and performing a
 50 more comprehensive analysis of the changes in their spectra
 51 with temperature.

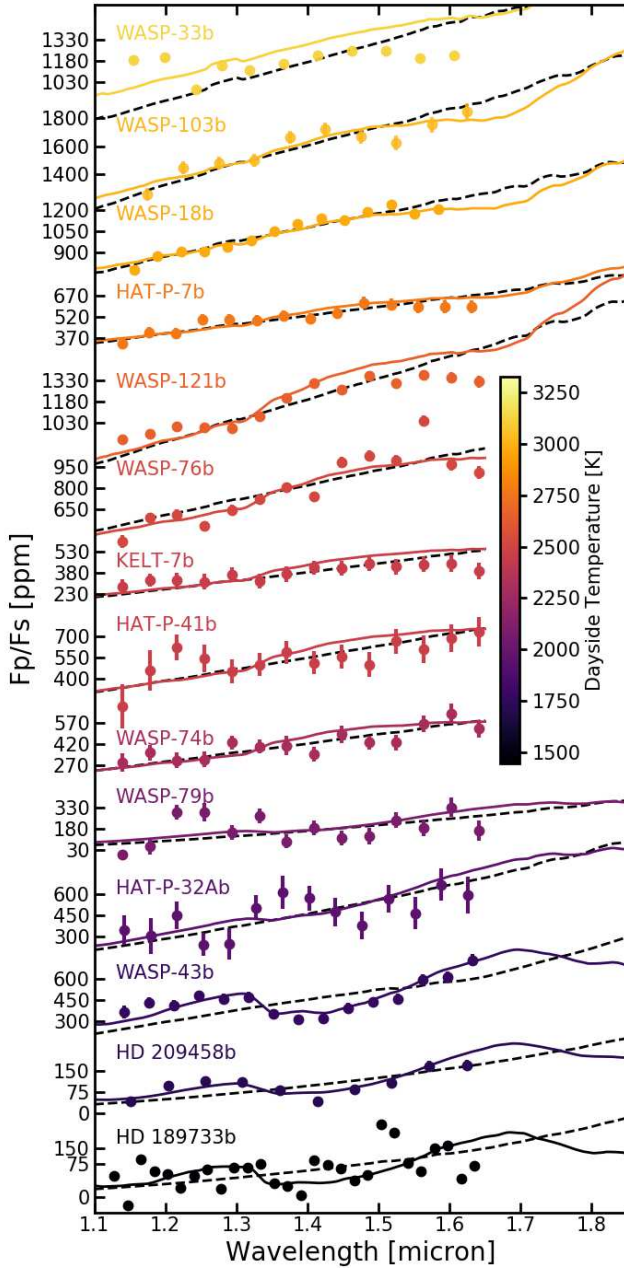


Figure 1. Secondary eclipse spectra for all 14 hot Jupiters considered in this study. Data sets are colored by dayside temperature, which is measured as described in the Methods and shown by the colorbar. Solid lines indicate interpolations from our solar composition fiducial model grid (see the Methods section for a description), while dashed lines indicate best-fit blackbodies. Note that for several data sets, the error bars are smaller than the point size.

We created a new grid of cloud-free irradiated 1D self-consistent radiative-convective-thermochemical equilibrium models to compare to the dayside *HST*/WFC3+G141 thermal emission observations. These models were created using the Sc-CHIMERA framework^{4,9,20-23} which includes a broad array of opacity sources that are important for the temperature range explored here, including atomic and ionic opacities that are relevant at the high temperatures of ultra-hot Jupiters²⁴. A full description of the models and complete list of opacities can be found in the Methods.

Figure 2 shows the temperature-pressure profiles and resultant secondary eclipse spectra for our fiducial model, which uses system parameters for a standard hot Jupiter (stellar effective temperature $T_{\text{eff}} = 5300$ K, planetary gravity $g = 10$ m/s², planetary metallicity $[\frac{M}{H}] = 0.0$, planetary carbon-to-oxygen abundance ratio $\frac{C}{O} = 0.55$, and planetary internal temperature $T_{\text{int}} = 150$ K). Models at different temperatures were created by scaling the incident stellar flux to match the specified irradiation temperature. Figure 2 also shows the ratio of the absorption mean opacity (κ_f) to the Planck mean opacity (κ_B) as a function of equilibrium temperature at a pressure of 10^{-2} bar, which is approximately the photospheric pressure in the *HST*/WFC3 bandpass (see the Methods for a full description of these opacities). This ratio describes the relative efficiency of stellar absorption vs. thermal re-radiation at that layer in the planet’s atmosphere²⁵.

In addition to the fiducial model grid, we created models with a variety of atmospheric/system parameters to see how individual parameters impact the 1D vertical structure and resulting population level trends observed in the dayside emission spectra. We examined models with stellar $T_{\text{eff}} = 3300$ K, 4300 K, 6300 K, 7200 K, and 8200 K; planetary gravity, $g = 1$ m/s² and 100 m/s²; metallicity, $[\frac{M}{H}] = -1.5$ and 1.5; and $\frac{C}{O} = 0.01$ and 0.85. We also included a model where the internal temperature varies with the planetary irradiation temperature to capture the internal entropy change that could be the cause of the hot Jupiter radii inflation²⁶. Furthermore, we tested models in which the TiO and VO opacity were removed *ad hoc* until temperatures above 2000 K, 2500 K, or 3000 K in order to simulate cold-trapping in cooler regions of the atmosphere^{3,27,28} (see the Methods section for a full description of these models). For all of these models, only one parameter was varied at a time while the other parameters were held fixed to the values in the fiducial model (e.g., a slice along a given parameter dimension).

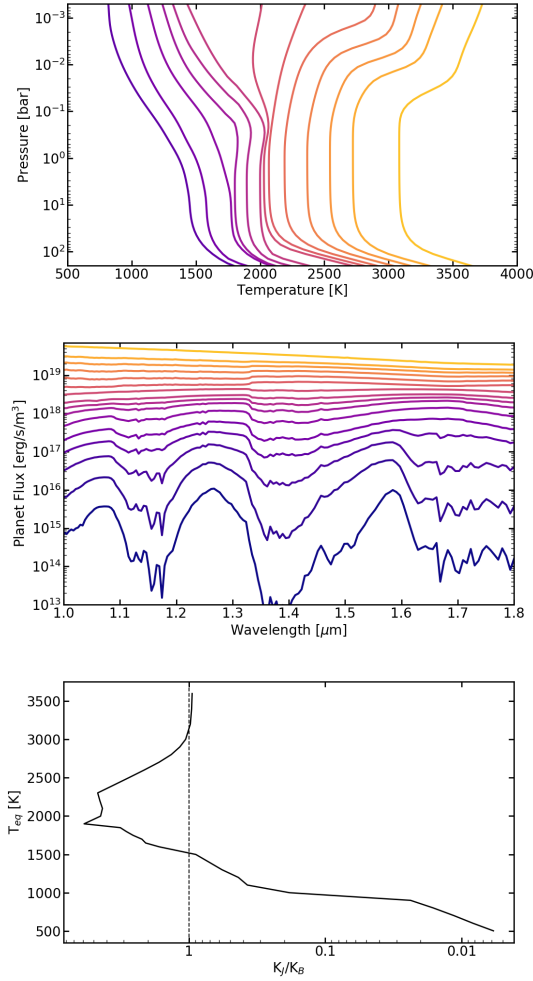


Figure 2. Temperature-pressure (T-P) profiles (top) and resulting dayside planet fluxes (middle) for the fiducial model grid, which covers approximately the same range of temperatures as spanned by the observations. The full model specifications are detailed in the Methods. The fiducial model uses a 5300 K stellar effective temperature, a solar composition planetary atmosphere ($[M/H] = 0.0$ and $C/O = 0.55$), a planetary gravity of 10 m/s^2 , and a planet internal temperature of 150 K. Blue and yellow lines show models with the coolest and warmest irradiation temperatures, respectively. For clarity, only every other model in the grid is shown here. The bottom panel shows the ratio of the absorption mean opacity (κ_J) to the Planck mean opacity (κ_B) as a function of equilibrium temperature in these models at a pressure of 10^{-2} bar. This ratio describes the relative efficiency of heating vs. cooling in the models²⁵, and a ratio of $\kappa_J/\kappa_B > 1$ generally indicates the presence of a thermal inversion in the temperature-pressure profile. This panel is plotted with temperature on the y-axis for ease of comparison to Figure 3.

98 the lowest dayside temperatures ($T_{\text{day}} < 2100 \text{ K}$ for the fiducial model), the models exhibit absorption features due to monotonically decreasing temperature profiles. At intermediate temperatures ($2100 \text{ K} < T_{\text{day}} < 3000 \text{ K}$ for the fiducial model), the modeled thermal structures exhibit a rising temperature with increasing altitude (decreasing pressure) due to the gas-phase onset of TiO and VO which push $\kappa_J/\kappa_B > 1$, in turn causing emission features. At the highest temperatures ($T_{\text{day}} > 3000 \text{ K}$ for the fiducial model), the models still show strong thermal inversions (becoming stronger primarily due to the dissociation of water, an efficient coolant) but the resulting secondary eclipse spectra are relatively featureless because of a combination of high-temperature effects such as molecular dissociation and the onset of H^- opacity, which cause all the WFC3+G141 wavelengths to probe the same altitude/pressure level, hence brightness temperature^{3,4,20,21,24}. The exact temperatures of the transitions between these regimes, as well as the strength of absorption and emission features present in the models, depend on the parameters of each set of models.

For both the models and the population of 14 observed hot Jupiters, we examined the degree of absorption or emission observed in the water feature at $1.4 \mu\text{m}$, the primary feature in the *HST*/WFC3+G141 bandpass. We quantified their deviation from a blackbody using an *HST* water feature strength metric, which is illustrated in Supplementary Figure 1. For each data set, we first fit a blackbody to the two “out-of-band” regions of the spectrum, which have wavelengths of $1.22 - 1.33 \mu\text{m}$ and $1.53 - 1.61 \mu\text{m}$ and are defined based on where the models in Figure 2 show minimal water opacity. The temperature of this blackbody is referred to throughout this paper as the observed dayside temperature (T_{day}) in this bandpass. The water feature strength is then defined as

$$S_{\text{H}_2\text{O}} = \log_{10} \left(\frac{F_{B,\text{in}}}{F_{\text{obs},\text{in}}} \right), \quad (1)$$

where $F_{B,\text{in}}$ and $F_{\text{obs},\text{in}}$ are the flux of the fitted blackbody and the observed data, respectively, in the “in-band” region shown in Supplementary Figure 1. The “in-band” wavelength region extends from $1.35 - 1.48 \mu\text{m}$ and captures the center of the primary water band observed in the *HST*/WFC3 bandpass. Supplementary Figure 2 shows all 14 secondary eclipse spectra with the “out-of-band” and “in-band” regions shaded. From this definition, $S_{\text{H}_2\text{O}}$ will have a positive value when a water feature is observed in absorption, a negative value when a feature is observed in emission, and a value of zero if a blackbody is observed.

Figures 3 and 4 show the observed *HST* water feature strengths for the sample of 14 hot Jupiter emission spectra compared to those of the models. Figure 3 shows that the observed *HST*/WFC3 feature strengths generally fall within the region of parameter space spanned by the models, with almost all of the planets fully within the predicted spread of the models. The models considered here assume elemental abundance ratios that fall within the range of commonly ex-

97 Our models predict three primary spectral regimes. At 148

pected outcomes from planet formation models^{14–17}. We find that varying parameters in these simple models can explain the observed hot Jupiter population without having to appeal to less likely outcomes of planet formation (e.g., $C/O > 1$ ^{14,15,17} or exotic chemistry.

Although the observed population of hot Jupiter emission spectra generally matches our model predictions, we find that no single model track can match all of the observations at better than a 6σ significance. This suggests there may be one or more parameters varying between the planets. To determine which parameters can most easily explain the scatter in the observed data, we examined the water feature strength variation we could achieve through changing each of our model parameters individually. Figure 4 shows water strengths for each individual model we examined. We found that the stellar effective temperature, planet gravity, and extent of internal heating had relatively small impacts on the predicted water feature strengths throughout the range of temperatures of the hot Jupiter population. Additionally, the models with TiO/VO opacity removed at different temperatures could only account for some of the scatter at intermediate temperatures and could not explain scatter at the highest or lowest temperatures, where we have observed the most precise secondary eclipse spectra. However, changing the atmospheric metallicity and C/O

ratio had a significant impact on the predicted *HST*/WFC3 water feature strengths. We found the observed scatter could be explained if the planets have atmospheric metallicities between 0.03 – 30x solar and C/O ratios between 0.01–0.85 (0.02 – 1.5x solar). Such variation is expected from planet formation models^{14,15} and has been suggested by a handful of transmission spectra studies (e.g.,¹⁷). The scatter we observed in emission spectra lends further support to the concept of compositional diversity among hot Jupiters.

Our hypothesis that hot Jupiters show compositional diversity can be tested through high-precision observations that cover more of the key O- and C-bearing molecules than are included in existing data sets (e.g. H₂O, CO, CO₂, and CH₄). Such observations will be possible with the upcoming *James Webb Space Telescope* (JWST)²⁹ and stabilized, high-resolution spectrographs on large ground-based telescopes that have broad wavelength coverage. Simultaneous detection of multiple molecules would lead to more precise constraints on metallicities and carbon-to-oxygen abundance ratios (and additional elemental ratios including nitrogen, etc.)². Beyond testing our hypothesis, more precise compositional constraints on exoplanet atmospheres would inform our understanding of the formation and evolution processes that have produced the diverse planetary systems revealed over the last 25 years.

References

1. Showman, A. P., Tan, X. & Parmentier, V. Atmospheric Dynamics of Hot Giant Planets and Brown Dwarfs. *arXiv e-prints* arXiv:2007.15363 (2020). [2007.15363](https://arxiv.org/abs/2007.15363).
2. Fortney, J. J., Lodders, K., Marley, M. S. & Freedman, R. S. A Unified Theory for the Atmospheres of the Hot and Very Hot Jupiters: Two Classes of Irradiated Atmospheres. *ApJ* **678**, 1419–1435 (2008). DOI 10.1086/528370. [0710.2558](https://doi.org/10.1086/528370).
3. Parmentier, V. *et al.* From thermal dissociation to condensation in the atmospheres of ultra hot Jupiters: WASP-121b in context. *A&A* **617**, A110 (2018). DOI 10.1051/0004-6361/201833059. [1805.00096](https://arxiv.org/abs/1805.00096).
4. Arcangeli, J. *et al.* H⁻ Opacity and Water Dissociation in the Dayside Atmosphere of the Very Hot Gas Giant WASP-18b. *ApJL* **855**, L30 (2018). DOI 10.3847/2041-8213/aab272. [1801.02489](https://arxiv.org/abs/1801.02489).
5. Kreidberg, L. *et al.* A Precise Water Abundance Measurement for the Hot Jupiter WASP-43b. *ApJL* **793**, L27 (2014). DOI 10.1088/2041-8205/793/2/L27. [1410.2255](https://arxiv.org/abs/1410.2255).
6. Mikal-Evans, T. *et al.* Confirmation of water emission in the dayside spectrum of the ultrahot Jupiter WASP-121b. *MNRAS* **496**, 1638–1644 (2020). DOI 10.1093/mnras/staa1628. [2005.09631](https://arxiv.org/abs/2005.09631).
7. Keating, D., Cowan, N. B. & Dang, L. Uniformly hot nightside temperatures on short-period gas giants. *Nat. Astron.* **3**, 1092–1098 (2019). DOI 10.1038/s41550-019-0859-z. [1809.00002](https://arxiv.org/abs/1809.00002).
8. Beatty, T. G. *et al.* Spitzer Phase Curves of KELT-1b and the Signatures of Nightside Clouds in Thermal Phase Observations. *AJ* **158**, 166 (2019). DOI 10.3847/1538-3881/ab33fc. [1808.09575](https://arxiv.org/abs/1808.09575).
9. Baxter, C. *et al.* A transition between the hot and the ultra-hot Jupiter atmospheres. *A&A* **639**, A36 (2020). DOI 10.1051/0004-6361/201937394. [2007.15287](https://arxiv.org/abs/2007.15287).
10. Garhart, E. *et al.* Statistical Characterization of Hot Jupiter Atmospheres Using Spitzer’s Secondary Eclipses. *AJ* **159**, 137 (2020). DOI 10.3847/1538-3881/ab6cff. [1901.07040](https://arxiv.org/abs/1901.07040).
11. Dransfield, G. & TriAUD, A. H. M. J. Colour-magnitude diagrams of transiting Exoplanets – III. A public code, nine strange planets, and the role of Phosphine. *arXiv e-prints* arXiv:2008.00995 (2020). [2008.00995](https://arxiv.org/abs/2008.00995).
12. Manjavacas, E. *et al.* Cloud Atlas: Hubble Space Telescope Near-infrared Spectral Library of Brown Dwarfs, Planetary-mass Companions, and Hot Jupiters. *AJ* **157**, 101 (2019). DOI 10.3847/1538-3881/aaf88f. [1812.03963](https://arxiv.org/abs/1812.03963).

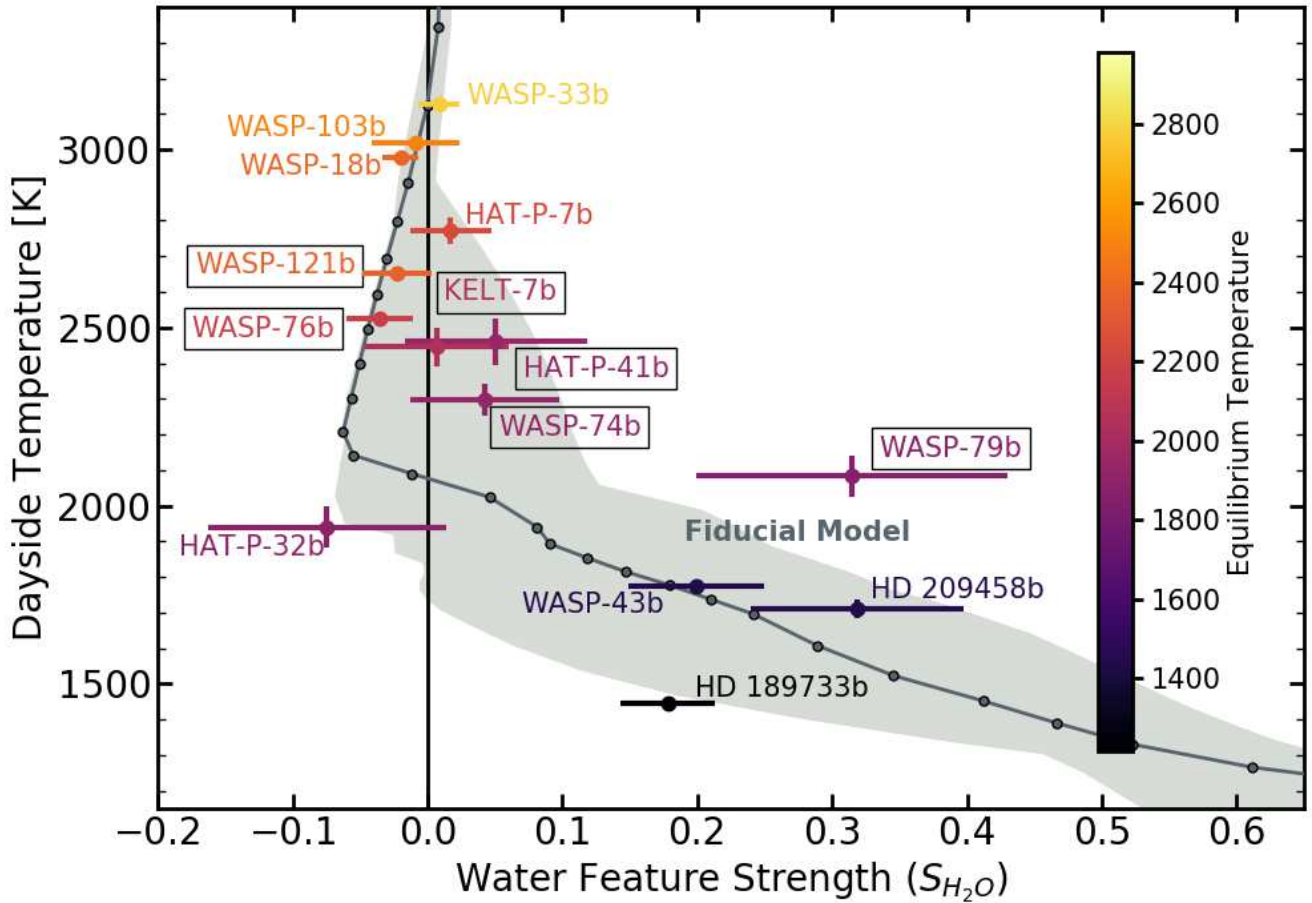


Figure 3. *HST* water feature strength diagram comparing observed secondary eclipse spectra to the model predictions in Figure 2. The y-axis shows the temperature of a blackbody fit to the “out-of-band” regions defined in Supplementary Figure 1, which is the observed dayside temperature T_{day} . The x-axis shows the strength of the observed feature in the water band at $1.4 \mu\text{m}$ compared to this blackbody, as defined by Equation 1. Featureless, blackbody-like spectra have $S_{H_2O} = 0$ and absorption/emission features have positive/negative colors, respectively. The gray line and points show the fiducial models pictured in Figure 2. The light gray shaded region shows the full range of model predictions assuming different values for the stellar effective temperature; the temperature where TiO opacity becomes important; and the planet gravity, C/O ratio, metallicity, and internal heat. Colored points with error bars show all planets with *HST*/WFC3 spectra observed in the spatial scanning mode, and boxes around planet names indicate new data reductions in this publication. The color scale indicates the planetary equilibrium temperature. The error bars include uncertainties in the stellar effective temperature.

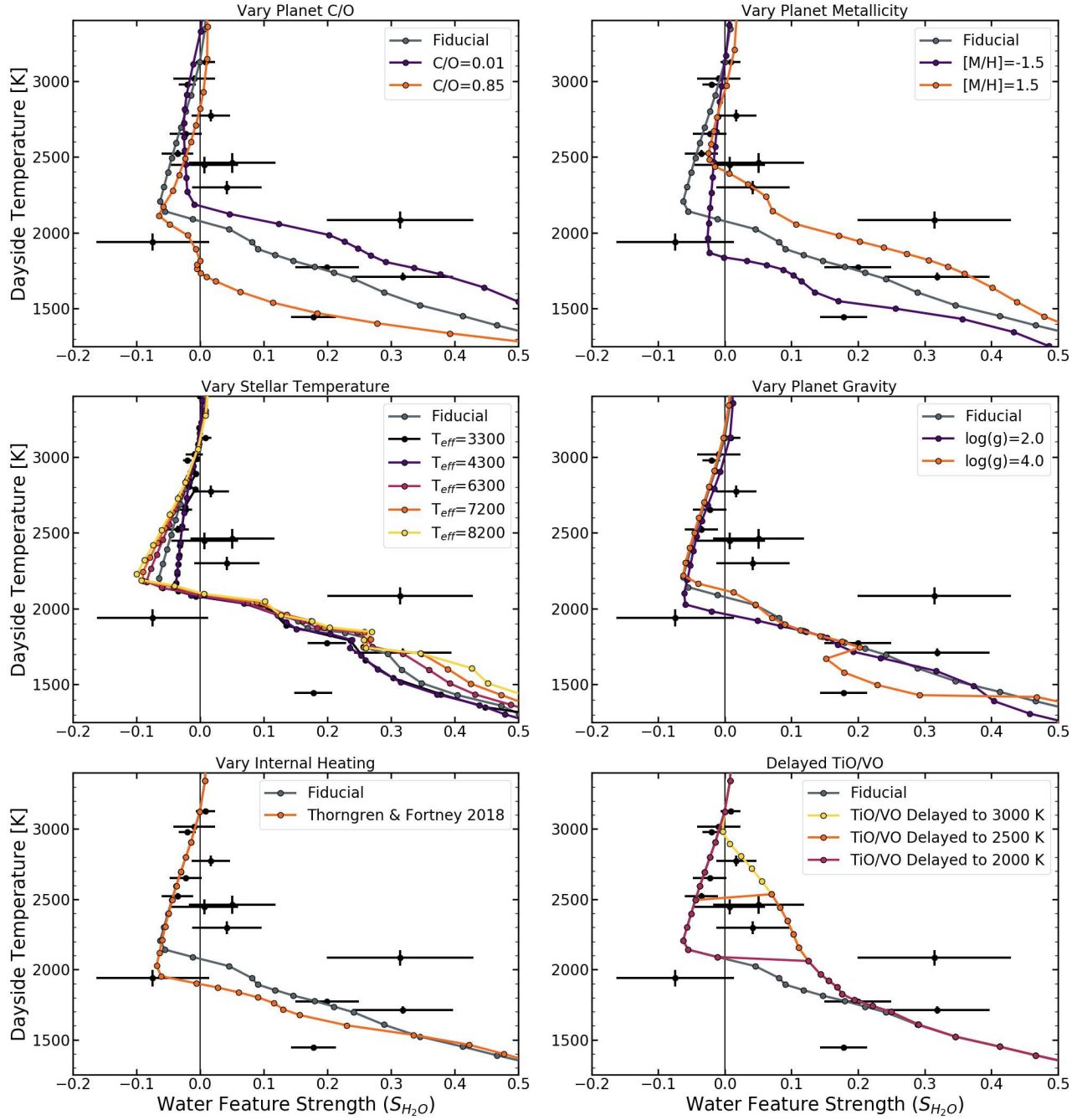


Figure 4. Diagrams illustrating the change in *HST* water feature strength from models with different parameters. All diagrams show the observed data as black points with error bars, while the lines show tracks for models with varying C/O ratio (top left), metallicity (top right), stellar temperature (middle left), gravity (middle right), internal heating (bottom left), and the temperature to which TiO opacity was ignored (bottom right). In each case all other parameters are held fixed at the fiducial model values. The error bars include uncertainties in the stellar effective temperature. We found that changing the stellar temperature, planetary gravity, and internal heating in our models had little impact on the derived water feature strengths, and changing the TiO/VO only had an impact at intermediate temperatures, but changing the atmospheric C/O ratio and metallicity can explain the diversity of observed secondary eclipse spectra.

- 222 **13.** Sing, D. K. *et al.* A continuum from clear to cloudy hot-Jupiter exoplanets without primordial water depletion. *Nat.* **529**,
223 59–62 (2016). DOI 10.1038/nature16068. [1512.04341](#).
- 224 **14.** Mordasini, C., van Boekel, R., Mollière, P., Henning, T. & Benneke, B. The Imprint of Exoplanet Formation History on
225 Observable Present-day Spectra of Hot Jupiters. *ApJ* **832**, 41 (2016). DOI 10.3847/0004-637X/832/1/41. [1609.03019](#).
- 226 **15.** Ali-Dib, M. Disentangling hot Jupiters formation location from their chemical composition. *MNRAS* **467**, 2845–2854
227 (2017). DOI 10.1093/mnras/stx260. [1611.03128](#).
- 228 **16.** Madhusudhan, N., Bitsch, B., Johansen, A. & Eriksson, L. Atmospheric signatures of giant exoplanet formation by pebble
229 accretion. *MNRAS* **469**, 4102–4115 (2017). DOI 10.1093/mnras/stx1139. [1611.03083](#).
- 230 **17.** Cridland, A. J., van Dishoeck, E. F., Alessi, M. & Pudritz, R. E. Connecting planet formation and astrochemistry. A
231 main sequence for C/O in hot exoplanetary atmospheres. *A&A* **632**, A63 (2019). DOI 10.1051/0004-6361/201936105.
232 [1910.13171](#).
- 233 **18.** Tsiaras, A. *et al.* A Population Study of Gaseous Exoplanets. *AJ* **155**, 156 (2018). DOI 10.3847/1538-3881/aaaf75.
234 [1704.05413](#).
- 235 **19.** Stevenson, K. B., Bean, J. L., Madhusudhan, N. & Harrington, J. Deciphering the Atmospheric Composition of WASP-
236 12b: A Comprehensive Analysis of its Dayside Emission. *ApJ* **791**, 36 (2014). DOI 10.1088/0004-637X/791/1/36.
237 [1406.7567](#).
- 238 **20.** Kreidberg, L. *et al.* Global Climate and Atmospheric Composition of the Ultra-hot Jupiter WASP-103b from HST and
239 Spitzer Phase Curve Observations. *AJ* **156**, 17 (2018). DOI 10.3847/1538-3881/aac3df. [1805.00029](#).
- 240 **21.** Mansfield, M. *et al.* An HST/WFC3 Thermal Emission Spectrum of the Hot Jupiter HAT-P-7b. *AJ* **156**, 10 (2018). DOI
241 10.3847/1538-3881/aac497. [1805.00424](#).
- 242 **22.** Piskorz, D. *et al.* Ground- and Space-based Detection of the Thermal Emission Spectrum of the Transiting Hot Jupiter
243 KELT-2Ab. *AJ* **156**, 133 (2018). DOI 10.3847/1538-3881/aad781. [1809.05615](#).
- 244 **23.** Zalesky, J. A., Line, M. R., Schneider, A. C. & Patience, J. A Uniform Retrieval Analysis of Ultra-cool Dwarfs. III.
245 Properties of Y Dwarfs. *ApJ* **877**, 24 (2019). DOI 10.3847/1538-4357/ab16db. [1903.11658](#).
- 246 **24.** Lothringer, J. D., Barman, T. & Koskinen, T. Extremely Irradiated Hot Jupiters: Non-oxide Inversions, H⁻ Opacity, and
247 Thermal Dissociation of Molecules. *ApJ* **866**, 27 (2018). DOI 10.3847/1538-4357/aadd9e. [1805.00038](#).
- 248 **25.** Lothringer, J. D. & Barman, T. The Influence of Host Star Spectral Type on Ultra-hot Jupiter Atmospheres. *ApJ* **876**, 69
249 (2019). DOI 10.3847/1538-4357/ab1485. [1903.12183](#).
- 250 **26.** Thorngren, D., Gao, P. & Fortney, J. J. The Intrinsic Temperature and Radiative-Convective Boundary Depth in the
251 Atmospheres of Hot Jupiters. *ApJL* **884**, L6 (2019). DOI 10.3847/2041-8213/ab43d0. [1907.07777](#).
- 252 **27.** Parmentier, V., Showman, A. P. & Lian, Y. 3D mixing in hot Jupiters atmospheres. I. Application to the day/night cold trap
253 in HD 209458b. *A&A* **558**, A91 (2013). DOI 10.1051/0004-6361/201321132. [1301.4522](#).
- 254 **28.** Beatty, T. G. *et al.* Evidence for Atmospheric Cold-trap Processes in the Noninverted Emission Spectrum of Kepler-13Ab
255 Using HST/WFC3. *AJ* **154**, 158 (2017). DOI 10.3847/1538-3881/aa899b. [1612.06409](#).
- 256 **29.** Greene, T. P. *et al.* Characterizing Transiting Exoplanet Atmospheres with JWST. *ApJ* **817**, 17 (2016). DOI 10.3847/0004-
257 637X/817/1/17. [1511.05528](#).
- 258 **30.** Snellen, I. A. G., de Kok, R. J., de Mooij, E. J. W. & Albrecht, S. The orbital motion, absolute mass and high-altitude
259 winds of exoplanet HD209458b. *Nat.* **465**, 1049–1051 (2010). DOI 10.1038/nature09111. [1006.4364](#).

260 **Methods**

261 **New Observations and Data Reduction**

262 We reduced and analyzed *HST*/WFC3+G141 spectra of six
263 planets. At the time this study was begun, these were all of
264 the remaining secondary eclipse data sets in the *HST* archive
265 that had not been published yet. Since we began this project,
266 results for three planets have been published^{6,31–33}. In all of
267 these cases, our reductions produced spectra consistent with
268 the published results. Supplementary Table 2 lists the details

269 of these observations, which included single eclipses of HAT-
270 P-41b, KELT-7b, WASP-74b, WASP-76b, and WASP-79b, as
271 well as five eclipses of WASP-121b.

We reduced the data using the data reduction pipeline
described in Kreidberg *et al.* (2014)³⁴. We used an optimal
extraction procedure³⁵ and masked cosmic rays. To subtract
the background out of each frame, we visually inspected the
images to find a clear background spot on the detector and
subtracted the median of this background area. The uncer-

278 tainties on the measurements were determined by adding in 330
 279 quadrature the photon noise, read noise, and median absolute 331
 280 deviation of the background. 332

281 Following standard procedure for *HST*/WFC3 eclipse ob-333
 282 servations, we discarded the first orbit of each visit. The 334
 283 spectra of each planet were binned into 14 channels at a reso-335
 284 lution $R \approx 30 - 40$. We also created a broadband white light 336
 285 curve for each planet by summing the spectra over the entire 337
 286 wavelength range. 338

287 We fit both the white light curves and spectroscopic light 339
 288 curves with a model in the form 340

$$M(t) = E(t)(cs + vt_{vis})(1 - e^{-r_1 t_{orb} - r_2}), \quad (2) \quad 341$$

289 where $M(t)$ is the modeled flux, $E(t)$ is an eclipse model found 343
 290 using `batman`³⁶, and the rest of the equation is a systematics 344
 291 model based on Berta et al. (2012)³⁷. In this systematics 345
 292 model, c is a normalization constant, s is a scaling factor to 346
 293 account for an offset in normalization between scan direc- 347
 294 tions, v is a visit-long linear trend, t_{vis} is the time since the 348
 295 beginning of the visit, r_1 and r_2 are the amplitude and time 349
 296 constant of an orbit-long exponential ramp, respectively, and 350
 297 t_{orb} is the time since the beginning of the orbit. For both the 351
 298 white light curves and the spectroscopic light curves, the only 352
 299 free parameter in the eclipse model was the planet-to-star flux 353
 300 ratio F_p/F_s . 354

301 The single eclipses observed for most of these planets 355
 302 had poor coverage of ingress and egress, so they could not 356
 303 constrain parameters such as the secondary eclipse time to the 357
 304 level of precision provided by previous observations. There- 358
 305 fore, all other eclipse parameters were fixed to the literature 359
 306 values listed in Supplementary Table 3. For the systematics 360
 307 model, c , v , and s were allowed to vary between orbits, while 361
 308 r_1 and r_2 were fixed to the same values for all orbits within a 362
 309 given visit. Four of the data sets (for HAT-P-41b, WASP-74b, 363
 310 WASP-79b, and WASP-121b) only used forward scanning 364
 311 instead of bi-directional scanning, so for these observations 365
 312 we fixed $s = 1$. The first secondary eclipse observation for 366
 313 WASP-121b occurred two years before the other four obser- 367
 314 vations and showed significant differences in the ramp shape, 368
 315 so we allowed this first eclipse to be fit with different values 369
 316 of r_1 and r_2 than the other four visits. 370

317 The data sets for WASP-76b and WASP-79b showed addi-371
 318 tional correlated noise after applying this systematic model, 372
 319 so for these two data sets we tested adding an additional 373
 320 quadratic term to the visit-long trend. While adding this ad-374
 321 ditional term was able to correct for the correlated noise, it 375
 322 introduced strong degeneracies between the fit parameters and 376
 323 the planet-to-star flux ratio. In order to avoid these degenera-377
 324 cies, we fit for only a linear visit-long trend in our final fit 378
 325 and used the divide-white method to correct for the additional 379
 326 noise³⁴. 380

327 We estimated the parameters with a Markov Chain Monte 381
 328 Carlo (MCMC) fit using the `emcee` package for Python³⁸. 382
 329 The final secondary eclipse spectra for all of the planets are 383

shown in Supplementary Figure 3, and the planet-to-star flux 384
 ratio in each wavelength bin is listed in Supplementary Ta- 385
 ble 4. The white light curves had reduced chi-squared values 386
 between $1.9 < \chi^2_v < 15.2$. The spectroscopic light curves 387
 generally achieved photon-limited precision, with $\approx 90\%$ of 388
 the light curves having reduced chi-squared values between 389
 $0.7 < \chi^2_v < 2.0$. However, occasional individual spectroscopic 390
 light curves had higher reduced chi-squared values between 391
 $2.0 < \chi^2_v < 3.4$. Therefore, before fitting each spectroscopic 392
 light curve we rescaled the uncertainties by a constant factor 393
 such that each light curve had $\chi^2_v = 1$ to give more conserva- 394
 tive error estimates. 395

WASP-76 has a companion star whose spectrum is 396
 blended with that of the primary star in the WFC3 data. We 397
 corrected for the presence of this companion star using the 398
 following equation: 399

$$F_{corr} = F_{obs} \left(1 + \frac{F_B}{F_A} \right), \quad (3) \quad 400$$

401 where F_{corr} is the corrected planet-to-star flux ratio in a given 402
 bandpass, F_{obs} is the observed flux ratio in that bandpass in- 403
 cluding the companion star contamination, F_B is the flux of 404
 the companion star in that bandpass, and F_A is the flux of the 405
 primary star in that bandpass. We used ATLAS models³⁹ with 406
 temperatures of 6250 K and 4824 K to represent the primary 407
 star and the companion star, respectively⁴⁰. 408

Observed Dayside Temperatures

409 As described in the main text, we measured the dayside tem- 410
 perature of each observed planet by fitting a blackbody to the 411
 “out-of-band” regions indicated in Supplementary Figure 1. 412
 Similar to previous studies⁴¹, we found a linear relationship 413
 between this observed dayside temperature and the planetary 414
 irradiation temperature given by 415

$$T_{day} = 0.807^{+0.008}_{-0.004} T_{irr} + 71^{+25}_{-8}, \quad (4) \quad 416$$

417 where $T_{irr} = T_{eff} \sqrt{R_*/a}$ is the irradiation temperature, R_* is 418
 the stellar radius, and a is the semi-major axis. 419

Model Grid

420 We created a new grid of self-consistent, 1D hot Jupiter 421
 models to compare their emission spectra to the popula- 422
 tion of observed planets. These models were generated us- 423
 ing the Sc-CHIMERA code (validated against established 424
 brown dwarf models⁴² and analytic models²²) assuming cloud- 425
 free, radiative-convective-thermochemical equilibrium atmo- 426
 spheres. The models’ assumption of chemical equilibrium 427
 is likely a good approximation for the highly irradiated plan- 428
 ets that make up the majority of our observed population⁴³. 429
 A two stream source function technique⁴⁴ is employed to 430
 solve for the planetary thermal fluxes at each atmospheric 431
 level (under the hemispheric mean approximation). We mod- 432
 eled the stellar flux via a standard two stream approximation 433
 (for both direct and diffuse fluxes, under the quadrature ap- 434
 proximation) assuming cosine incident angle of 0.5, utilizing 435

the PHOENIX models for the stellar spectra⁴⁵. A Newton-Raphson iteration⁴⁶ is used to determine the temperature at each model layer which ensures zero net flux divergence. We include absorption cross-sections from 0.1 - 100 μm (where available) for H_2O , CO , CO_2 , CH_4 , NH_3 , H_2S , PH_3 , HCN , C_2H_2 , TiO , VO , SiO , FeH , CaH , MgH , CrH , AlH , Na , K , Fe , Mg , Ca , C , Si , Ti , O , Fe^+ , Mg^+ , Ti^+ , Ca^+ , C^+ , H_2 , $\text{H}_2\text{-H}_2/\text{He}$ CIA,⁴⁷⁻⁵⁰ H^- bound-free and free-free^{51,52}, and H_2/He Rayleigh scattering, and additional UV opacities for CO , SiO , and H_2 ⁴⁹. Pre-computed cross-sections were converted into correlated-K coefficients at a spectral resolution of 250 using a 10 point double Gauss quadrature (with half covering the top 5% of the correlated-K cumulative distribution function) with mixed-gas optical depths computed using the random-overlap resort-rebin framework (e.g.,^{53,54}). Thermochemical equilibrium molecular abundances were computed using the NASA CEA Gibbs free energy minimization code⁵⁵ combined with elemental-rain out due to condensate formation (all major Si, Fe, Mg, Ca, Al, Na, and K bearing condensates are included) given the Lodders et al. (2009)⁵⁶ elemental abundances.

We parameterized the model atmospheres with a set of five parameters: the stellar effective temperature (T_{eff}), the planetary gravity (g), the planetary metallicity ($[\frac{\text{M}}{\text{H}}]$), the planetary carbon-to-oxygen ratio ($\frac{\text{C}}{\text{O}}$), and the planetary internal temperature (T_{int}). Our fiducial models had the following parameter values: $T_{\text{eff}} = 5300 \text{ K}$, $g = 10 \text{ m/s}^2$, $[\frac{\text{M}}{\text{H}}] = 0.0$, $\frac{\text{C}}{\text{O}} = 0.55$, $T_{\text{int}} = 150 \text{ K}$. Models at different irradiation temperatures were created by re-scaling the incident stellar spectrum (the PHOENIX model for a given stellar effective temperature) by the ratio of the desired irradiation temperature to the bolometric temperature of a planet at 0.05 AU around a 1 solar radius star. We created models with irradiation temperatures between 500 – 3600 K, with step sizes of 50 – 200 K.

Following Lothringer & Barman (2019)²⁵, we calculate the absorption mean opacity κ_J and the Planck mean opacity κ_B at a pressure of 10^{-2} bar as a function of equilibrium temperature for our fiducial models. The absorption mean opacity at a given pressure P is given by

$$\kappa_J(P) = \frac{\int_0^\infty \kappa_\lambda(T, P) J_\lambda(P) d\lambda}{\int_0^\infty J_\lambda(P) d\lambda}, \quad (5)$$

where κ_λ is the monochromatic true absorption coefficient, J_λ is the mean intensity at a given wavelength, and T is the local temperature in the planet's atmosphere²⁵. The Planck mean opacity is given by

$$\kappa_B(P) = \frac{\int_0^\infty \kappa_\lambda(T, P) B_\lambda(T) d\lambda}{\int_0^\infty B_\lambda(T) d\lambda}, \quad (6)$$

where $B_\lambda(T)$ is the Planck function. The ratio κ_J/κ_B describes the relative efficiency of stellar absorption vs. thermal re-radiation, and a ratio $\kappa_J/\kappa_B > 1$ generally indicates the presence of a thermal inversion in the temperature-pressure profile.

We also created subset grids as a function of irradiation temperature where a single parameter dimension was varied while all other parameters were held fixed to their fiducial model values (no cross-variance). We examined models with a stellar $T_{\text{eff}} = 3300 \text{ K}$, 4300 K, 6300 K, 7200 K, and 8200 K; $g = 1 \text{ m/s}^2$ and 100 m/s^2 ; $[\frac{\text{M}}{\text{H}}] = -1.5$ and 1.5 ; and $\frac{\text{C}}{\text{O}} = 0.01$ and 0.85 . For models with different metallicities, elemental abundance ratios were held constant while the overall metallicity was re-scaled relative to H. We also created a model grid where the internal temperature varies with the planetary irradiation temperature following Equation 3 in ref⁽²⁶⁾. Individual model tracks with irradiation temperature for each of these variations are shown in Figure 4.

Opacity from gaseous TiO/VO is theorized to be a driving force behind the transition between uninverted hot Jupiter atmospheres with monotonically decreasing temperature-pressure profiles and atmospheres containing thermal inversions². Some previous observations of hot Jupiters have suggested that vapor TiO/VO may not be present in high-temperature atmospheres if it is condensed in cooler parts of the atmosphere (e.g.,²⁸). This process, known as cold-trapping, effectively works to remove TiO/VO from places in the atmosphere where vaporized TiO/VO would be expected to be present in equilibrium. In order to study the impact of potential cold-trapping, we created models where the TiO and VO opacities are artificially set to zero until a given temperature threshold. We tested models where TiO/VO opacity is zeroed out for temperatures below 2000 K, 2500 K, and 3000 K. These tracks are also shown in Figure 4.

Recent studies have suggested clouds may have an impact on the strength of molecular absorption features observed in thermal emission (e.g.,^{7,57}). To test the impact the presence of clouds would have on the trends in our models, we created two cloudy models. We used the cloud model of Ackerman & Marley (2001)⁵⁸, as implemented by Mai & Line (2019)⁵⁹. Both models had a constant vertical mixing strength of $10^8 \text{ cm}^2/\text{s}$ using the Zahnle et al. (2016)⁶⁰ timescale prescription. We tested models with sedimentation efficiencies of $f_{\text{sed}} = 0.1$ and 1.0 . These models are shown compared to the fiducial model in Supplementary Figure 4. Adding clouds acts to weaken the water feature strengths below a dayside temperature of about 2000 K, with a smaller f_{sed} leading to more effective weakening. While clouds may provide a potential explanation for the weak water feature strength of HD 189733b, the lowest-temperature hot Jupiter in our population study, we find that including clouds can not generally explain the scatter we see in water feature strengths and has no impact on the feature strengths above $T_{\text{day}} = 2000 \text{ K}$. Our results agree with those from general circulation models, which also show that clouds have little to no impact at temperatures above $\approx 2000 \text{ K}$ ^{61,62}.

477 **Data Availability Statement**

480 The model grid can be found [online](#).

478 Data that support this paper’s findings and its plots are avail-
479 able from the corresponding author upon reasonable request.

481 **Correspondence and Requests**

482 Correspondence and requests for materials should be addressed to M.M.

483 **Acknowledgements**

484 Based on observations made with the NASA/ESA Hubble Space Telescope, obtained from the data archive at the Space
485 Telescope Science Institute. STScI is operated by the Association of Universities for Research in Astronomy, Inc. under NASA
486 contract NAS 5-26555. M.M. acknowledges funding from a NASA FINESST grant. M.R.L acknowledges funding from NSF
487 AST-165220, and NASA NNX17AB56G. M.R.L also acknowledges opacity information from Roxana Lupu and Ehsan-Gharib
488 Nezhad. M.R.L., J.L.B., and J.J.F. acknowledge funding for this work from STScI grants GO-13467 and GO-14792. J.M.D
489 acknowledges support from the Amsterdam Academic Alliance (AAA) Program, and the European Research Council (ERC)
490 European Union’s Horizon 2020 research and innovation programme (grant agreement no. 679633; Exo-Atmos). This work is
491 part of the research programme VIDI New Frontiers in Exoplanetary Climatology with project number 614.001.601, which is
492 (partly) financed by the Dutch Research Council (NWO).

493 **Author contributions statement**

494 M.M. reduced and analyzed the new data sets, led the data-model comparison, and wrote the manuscript. M.R.L. created the
495 self-consistent 1D model grids and contributed to the writing of the manuscript. J.L.B. contributed to the conception of the
496 population study and the writing of the manuscript. J.J.F. contributed to the interpretation of the results and the writing of the
497 manuscript. V.P., E.M.-R.K., C.B., and J.-M.D. contributed to the interpretation of the results. D.K.S. and M.L.-M. are PIs of
498 the *HST* program GO-14767 from which we obtained the new observations that were analyzed in this work. M.R.S. and G.M.R.
499 contributed to the conception of the population study. All authors commented on the manuscript.

500 **Facilities:** Hubble Space Telescope, Wide Field Camera 3

501 **Software:** [batman](#)³⁶, [emcee](#)³⁸, [matplotlib](#)⁶³, [numpy](#)⁶⁴, [pysynphot](#)⁶⁵, [scipy](#)⁶⁶

502 **Competing Interests**

503 The authors declare no competing financial interests.

504 **Supplementary Information References**

505 **31.** Edwards, B. *et al.* ARES I: WASP-76 b, A Tale of Two HST Spectra. *AJ* **160**, 8 (2020). DOI 10.3847/1538-3881/ab9225.
506 [2005.02374](#).

507 **32.** Fu, G. *et al.* The Hubble PanCET program: Transit and Eclipse Spectroscopy of the Strongly Irradiated Giant Exoplanet
508 WASP-76b. *arXiv e-prints* arXiv:2005.02568 (2020). [2005.02568](#).

509 **33.** Pluriel, W. *et al.* ARES. III. Unveiling the Two Faces of KELT-7 b with HST WFC3. *AJ* **160**, 112 (2020). DOI
510 10.3847/1538-3881/aba000. [2006.14199](#).

511 **34.** Kreidberg, L. *et al.* Clouds in the atmosphere of the super-Earth exoplanet GJ1214b. *Nat.* **505**, 69–72 (2014). DOI
512 10.1038/nature12888. [1401.0022](#).

513 **35.** Horne, K. An optimal extraction algorithm for CCD spectroscopy. *PASP* **98**, 609–617 (1986). DOI 10.1086/131801.

514 **36.** Kreidberg, L. *batman*: BASic Transit Model cAlculatioN in Python. *PASP* **127**, 1161 (2015). DOI 10.1086/683602.
515 [1507.08285](#).

516 **37.** Berta, Z. K. *et al.* The Flat Transmission Spectrum of the Super-Earth GJ1214b from Wide Field Camera 3 on the Hubble
517 Space Telescope. *ApJ* **747**, 35 (2012). DOI 10.1088/0004-637X/747/1/35. [1111.5621](#).

518 **38.** Foreman-Mackey, D., Hogg, D. W., Lang, D. & Goodman, J. *emcee*: The MCMC Hammer. *PASP* **125**, 306 (2013). DOI
519 10.1086/670067. [1202.3665](#).

520 **39.** Castelli, F. & Kurucz, R. L. New Grids of ATLAS9 Model Atmospheres. In Piskunov, N., Weiss, W. W. & Gray, D. F.
521 (eds.) *Modelling of Stellar Atmospheres*, vol. 210 of *IAU Symposium*, A20 (2003). [astro-ph/0405087](#).

- 522 **40.** Southworth, J., Bohn, A. J., Kenworthy, M. A., Ginski, C. & Mancini, L. A multiplicity study of transiting exoplanet host
523 stars. II. Revised properties of transiting planetary systems with companions. *A&A* **635**, A74 (2020). DOI 10.1051/0004-
524 6361/201937334. [2001.08225](#).
- 525 **41.** Schwartz, J. C. & Cowan, N. B. Balancing the energy budget of short-period giant planets: evidence for reflective clouds
526 and optical absorbers. *MNRAS* **449**, 4192–4203 (2015). DOI 10.1093/mnras/stv470. [1502.06970](#).
- 527 **42.** Saumon, D. & Marley, M. S. The Evolution of L and T Dwarfs in Color-Magnitude Diagrams. *ApJ* **689**, 1327–1344
528 (2008). DOI 10.1086/592734. [0808.2611](#).
- 529 **43.** Kitzmann, D. *et al.* The Peculiar Atmospheric Chemistry of KELT-9b. *ApJ* **863**, 183 (2018). DOI 10.3847/1538-
530 4357/aace5a. [1804.07137](#).
- 531 **44.** Toon, O. B., McKay, C. P., Ackerman, T. P. & Santhanam, K. Rapid calculation of radiative heating rates and
532 photodissociation rates in inhomogeneous multiple scattering atmospheres. *JGR* **94**, 16287–16301 (1989). DOI
533 10.1029/JD094iD13p16287.
- 534 **45.** Husser, T. O. *et al.* A new extensive library of PHOENIX stellar atmospheres and synthetic spectra. *A&A* **553**, A6 (2013).
535 DOI 10.1051/0004-6361/201219058. [1303.5632](#).
- 536 **46.** McKay, C. P., Pollack, J. B. & Courtin, R. The thermal structure of Titan’s atmosphere. *Icarus* **80**, 23–53 (1989). DOI
537 10.1016/0019-1035(89)90160-7.
- 538 **47.** Lupu, R. E. *et al.* The Atmospheres of Earthlike Planets after Giant Impact Events. *ApJ* **784**, 27 (2014). DOI 10.1088/0004-
539 637X/784/1/27. [1401.1499](#).
- 540 **48.** Tennyson, J. *et al.* The 2020 release of the ExoMol database: molecular line lists for exoplanet and other hot atmospheres.
541 *arXiv e-prints* arXiv:2007.13022 (2020). [2007.13022](#).
- 542 **49.** Kurucz, R. & Bell, B. Atomic Line Data. *At. Line Data (R.L. Kurucz B. Bell) Kurucz CD-ROM No. 23. Camb.* **23** (1995).
543
- 544 **50.** Gharib-Nezhad, E. & Line, M. R. The Influence of H₂O Pressure Broadening in High-metallicity Exoplanet Atmospheres.
544 *ApJ* **872**, 27 (2019). DOI 10.3847/1538-4357/aafb7b. [1809.02548](#).
- 545 **51.** Bell, K. L. & Berrington, K. A. Free-free absorption coefficient of the negative hydrogen ion. *J. Phys. B: At.* **20**, 1 (1987).
546
- 547 **52.** John, T. L. Continuous absorption by the negative hydrogen ion reconsidered. *A&A* **193**, 189–192 (1988).
548
- 549 **53.** Lacis, A. A. & Oinas, V. A description of the correlated-k distribution method for modelling nongray gaseous absorption,
548 thermal emission, and multiple scattering in vertically inhomogeneous atmospheres. *JGR* **96**, 9027–9064 (1991). DOI
549 10.1029/90JD01945.
- 550 **54.** Amundsen, D. S. *et al.* The UK Met Office global circulation model with a sophisticated radiation scheme applied to the
551 hot Jupiter HD 209458b. *A&A* **595**, A36 (2016). DOI 10.1051/0004-6361/201629183. [1608.08593](#).
- 552 **55.** Gordon, S. & Mcbride, B. J. Computer program for calculation of complex chemical equilibrium compositions and
553 applications. part I: Analysis. Tech. Rep. 19950013764, NASA Lewis Research Center (1994).
- 554 **56.** Lodders, K., Palme, H. & Gail, H. P. Abundances of the Elements in the Solar System. *Landolt Börnstein* **4B**, 712 (2009).
555 [0901.1149](#).
- 556 **57.** Taylor, J. *et al.* How Does Thermal Scattering Shape the Infrared Spectra of Cloudy Exoplanets? A Theoretical Framework
557 and Consequences for Atmospheric Retrievals in the JWST era. *arXiv e-prints* arXiv:2009.12411 (2020). [2009.12411](#).
- 558 **58.** Ackerman, A. S. & Marley, M. S. Precipitating Condensation Clouds in Substellar Atmospheres. *ApJ* **556**, 872–884
559 (2001). DOI 10.1086/321540. [astro-ph/0103423](#).
- 560 **59.** Mai, C. & Line, M. R. Exploring Exoplanet Cloud Assumptions in JWST Transmission Spectra. *ApJ* **883**, 144 (2019).
561 DOI 10.3847/1538-4357/ab3e6d. [1908.10904](#).
- 562 **60.** Zahnle, K., Marley, M. S., Morley, C. V. & Moses, J. I. Photolytic Hazes in the Atmosphere of 51 Eri b. *ApJ* **824**, 137
563 (2016). DOI 10.3847/0004-637X/824/2/137. [1604.07388](#).
- 564 **61.** Roman, M. T. *et al.* Clouds in Three-Dimensional Models of Hot Jupiters Over a Wide Range of Temperatures I: Thermal
565 Structures and Broadband Phase Curve Predictions. *arXiv e-prints* arXiv:2010.06936 (2020). [2010.06936](#).
- 566 **62.** Parmentier, V., Showman, A. P. & Fortney, J. J. The cloudy shape of hot Jupiter thermal phase curves. *arXiv e-prints*
567 arXiv:2010.06934 (2020). [2010.06934](#).

- 568 **63.** Hunter, J. D. Matplotlib: A 2d graphics environment. *Comput. In Sci. & Eng.* **9**, 90–95 (2007). DOI
569 10.1109/MCSE.2007.55.
- 570 **64.** van der Walt, S., Colbert, S. C. & Varoquaux, G. The NumPy Array: A Structure for Efficient Numerical Computation.
571 *Comput. Sci. Eng.* **13**, 22–30 (2011). DOI 10.1109/MCSE.2011.37. [1102.1523](#).
- 572 **65.** STScI Development Team. pynphot: Synthetic photometry software package (2013). [1303.023](#).
- 573 **66.** Virtanen, P. *et al.* SciPy 1.0—Fundamental Algorithms for Scientific Computing in Python. *arXiv e-prints* arXiv:1907.10121
574 (2019). [1907.10121](#).
- 575 **67.** Bean, J. L. *et al.* Remastering the classics: A thermal inversion for the hot Jupiter archetype HAT-P-7b? HST Proposal
576 (2016).
- 577 **68.** Sing, D. K. *et al.* The Panchromatic Comparative Exoplanetary Treasury Program. HST Proposal (2016).
- 578 **69.** Nikolov, N. *et al.* Hubble PanCET: an isothermal day-side atmosphere for the bloated gas-giant HAT-P-32Ab. *MNRAS*
579 **474**, 1705–1717 (2018). DOI 10.1093/mnras/stx2865. [1711.00859](#).
- 580 **70.** McCullough, P. Spanning the chasms: re-observing the transiting exoplanet HD 189733b. HST Proposal (2012).
- 581 **71.** Crouzet, N., McCullough, P. R., Deming, D. & Madhusudhan, N. Water Vapor in the Spectrum of the Extrasolar Planet
582 HD 189733b. II. The Eclipse. *ApJ* **795**, 166 (2014). DOI 10.1088/0004-637X/795/2/166. [1409.4000](#).
- 583 **72.** Bean, J. Follow The Water: The Ultimate WFC3 Exoplanet Atmosphere Survey. HST Proposal (2013).
- 584 **73.** Line, M. R. *et al.* No Thermal Inversion and a Solar Water Abundance for the Hot Jupiter HD 209458b from HST/WFC3
585 Spectroscopy. *AJ* **152**, 203 (2016). DOI 10.3847/0004-6256/152/6/203. [1605.08810](#).
- 586 **74.** Zhao, M. Near-IR spectroscopy of the newly discovered benchmark hot Jupiter WASP-103b. HST Proposal (2014).
- 587 **75.** Kreidberg, L. *et al.* Exploring the Frontier of Exoplanet Atmosphere Dynamics with NASA’s Great Observatories. Spitzer
588 Proposal (2014).
- 589 **76.** Evans, T. A global map of thermal inversions for an ultra-hot planet. HST Proposal (2017).
- 590 **77.** Stassun, K. G., Collins, K. A. & Gaudi, B. S. Accurate Empirical Radii and Masses of Planets and Their Host Stars with
591 Gaia Parallaxes. *AJ* **153**, 136 (2017). DOI 10.3847/1538-3881/aa5df3. [1609.04389](#).
- 592 **78.** Johnson, M. C., Cochran, W. D., Addison, B. C., Tinney, C. G. & Wright, D. J. Spin-Orbit Misalignments of Three Jovian
593 Planets via Doppler Tomography. *AJ* **154**, 137 (2017). DOI 10.3847/1538-3881/aa8462. [1708.01291](#).
- 594 **79.** Zhou, G. *et al.* Spin-orbit alignment for KELT-7b and HAT-P-56b via Doppler tomography with TRES. *MNRAS* **460**,
595 3376–3383 (2016). DOI 10.1093/mnras/stw1107. [1605.01991](#).
- 596 **80.** Bonomo, A. S. *et al.* The GAPS Programme with HARPS-N at TNG . XIV. Investigating giant planet migration history via
597 improved eccentricity and mass determination for 231 transiting planets. *A&A* **602**, A107 (2017). DOI 10.1051/0004-
598 6361/201629882. [1704.00373](#).
- 599 **81.** West, R. G. *et al.* Three irradiated and bloated hot Jupiters: WASP-76b, WASP-82b, and WASP-90b. *A&A* **585**, A126
600 (2016). DOI 10.1051/0004-6361/201527276. [1310.5607](#).
- 601 **82.** Delrez, L. *et al.* WASP-121 b: a hot Jupiter close to tidal disruption transiting an active F star. *MNRAS* **458**, 4025–4043
602 (2016). DOI 10.1093/mnras/stw522. [1506.02471](#).

603 **Supplementary Tables**

Planet	<i>HST</i> Program #	Number of Eclipses	Literature Reference
HAT-P-7b	14792 ⁶⁷	2	Mansfield et al. (2018) ²¹
HAT-P-32Ab	14767 ⁶⁸	1	Nikolov et al. (2018) ⁶⁹
HD 189733b	12881 ⁷⁰	1	Crouzet et al. (2014) ⁷¹
HD 209458b	13467 ⁷²	5	Line et al. (2016) ⁷³
WASP-18b	13467 ⁷²	5	Arcangeli et al. (2018) ⁴
WASP-43b	13467 ⁷²	5	Kreidberg et al. (2014) ⁵
WASP-103b	13660 ⁷⁴ , 14050 ⁷⁵	4	Kreidberg et al. (2018) ²⁰

Supplementary Table 1. Literature references and *HST* program numbers for the eight planets whose spectra were taken from the existing literature.

Planet	<i>HST</i> Program #	Date(s) of Observation	Sampling Sequence	Exposure Time [s]	Exposures per Orbit
HAT-P-41b	14767(1) ⁶⁸	10/09/16	SPARS10, NSAMP=12	81.089	19
KELT-7b	14767(1) ⁶⁸	08/18/17	SPARS10, NSAMP=4	22.317	37
WASP-74b	14767(1) ⁶⁸	05/02/17	SPARS25, NSAMP=4	69.617	19
WASP-76b	14767(1) ⁶⁸	11/03/16	SPARS10, NSAMP=15	103.129	19
WASP-79b	14767(1) ⁶⁸	11/15/16	SPARS25, NSAMP=7	138.381	13
WASP-121b	14767(1) ⁶⁸ , 15134(4) ⁷⁶	11/10/16-11/11/16, 03/12/18-03/13/18, 03/14/18, 02/03/19, 02/04/19	SPARS10, NSAMP=15	103.129	16

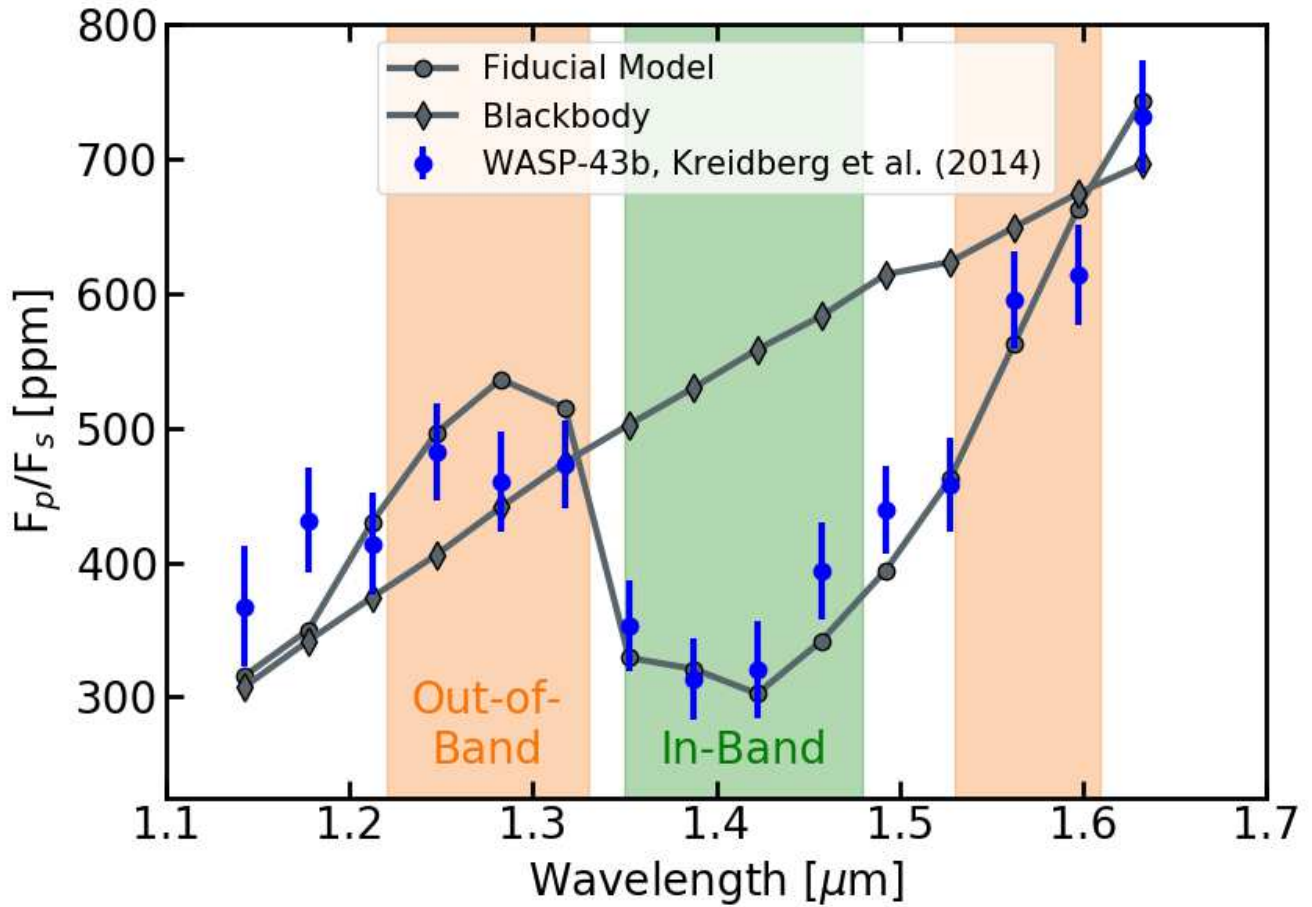
Supplementary Table 2. Observing details for the six planets for which new data reductions were performed in this work. Numbers in parentheses next to the *HST* program number indicate the number of eclipses observed in that program.

Planet	Period [days]	Mid-Transit Time [BJD]	a/r_*	Inclination [°]	r_p/r_*
HAT-P-41b	2.694050 ⁷⁷	2454983.8617 ⁷⁸	5.45 ⁷⁷	87.70 ⁷⁷	0.1028 ⁷⁸
KELT-7b	2.734770 ⁷⁷	2456355.2293 ⁷⁹	5.50 ⁷⁷	83.76 ⁷⁷	0.0888 ³³
WASP-74b	2.137750 ⁷⁷	2456506.8926 ⁸⁰	4.86 ⁷⁷	79.81 ⁷⁷	0.0980 ⁷⁷
WASP-76b	1.809882 ³²	2456107.8551 ⁸¹	4.08 ³²	88.50 ³²	0.1087 ³²
WASP-79b	3.662380 ⁷⁷	2455545.2361 ⁸⁰	7.03 ⁷⁷	85.40 ⁷⁷	0.1049 ⁷⁷
WASP-121b	1.274926 ⁸²	2456635.7083 ⁸²	3.75 ⁸²	87.60 ⁸²	0.1245 ⁸²

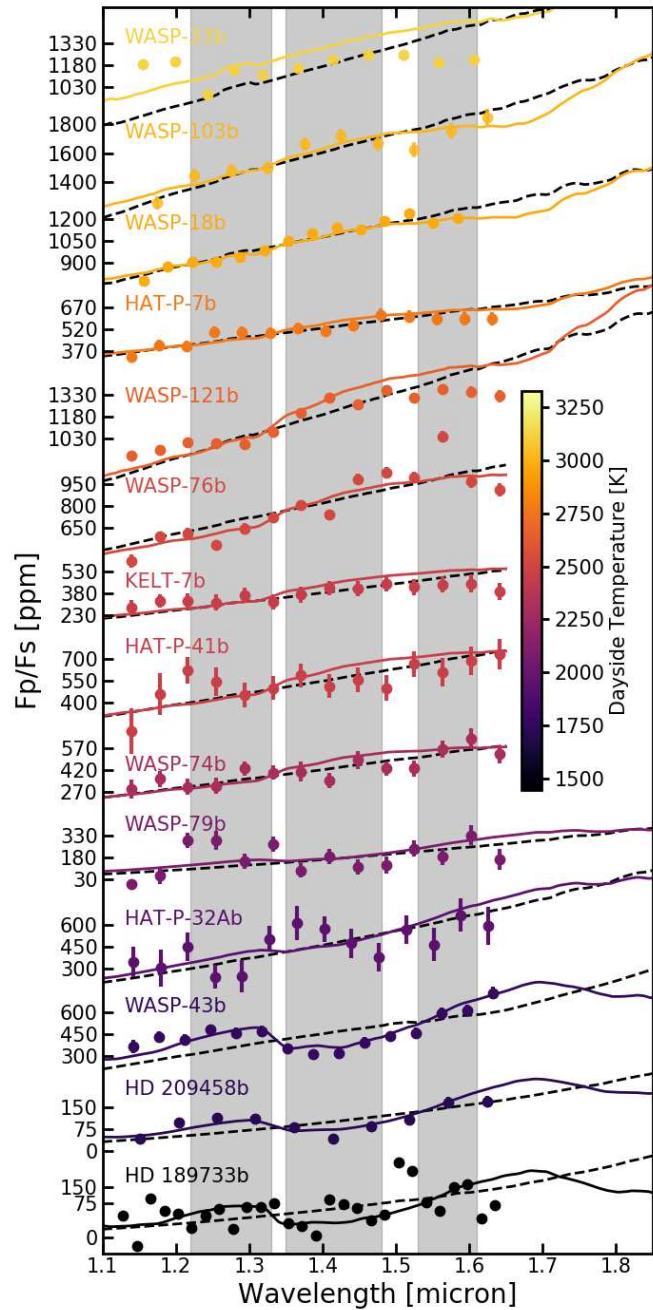
Supplementary Table 3. Literature values for fixed eclipse parameters in the light curve models for the six data sets reduced in this work.

Wavelength [μm]	HAT-P-41b	KELT-7b	WASP-74b	WASP-76b	WASP-79b	WASP-121b
1.120 – 1.159	207 ± 157	284 ± 51	288 ± 67	424 ± 44	12 ± 33	914 ± 32
1.159 – 1.197	461 ± 140	328 ± 45	357 ± 54	589 ± 33	58 ± 60	956 ± 32
1.197 – 1.236	622 ± 91	328 ± 49	304 ± 57	614 ± 37	297 ± 54	1009 ± 33
1.236 – 1.274	545 ± 95	318 ± 54	310 ± 55	533 ± 35	298 ± 64	1001 ± 29
1.274 – 1.313	452 ± 84	368 ± 48	429 ± 48	645 ± 35	155 ± 49	996 ± 30
1.313 – 1.351	503 ± 79	321 ± 50	401 ± 50	723 ± 33	272 ± 54	1079 ± 32
1.351 – 1.390	590 ± 81	371 ± 54	407 ± 67	804 ± 33	92 ± 50	1206 ± 30
1.390 – 1.429	515 ± 82	415 ± 51	346 ± 50	739 ± 36	186 ± 52	1309 ± 31
1.429 – 1.467	561 ± 84	411 ± 53	486 ± 59	980 ± 37	116 ± 53	1266 ± 31
1.467 – 1.506	501 ± 87	445 ± 55	428 ± 51	1027 ± 35	130 ± 58	1362 ± 32
1.506 – 1.544	666 ± 89	424 ± 56	428 ± 53	993 ± 37	242 ± 57	1311 ± 36
1.544 – 1.583	613 ± 96	439 ± 56	560 ± 56	1273 ± 40	185 ± 59	1370 ± 36
1.583 – 1.621	687 ± 96	447 ± 64	633 ± 71	970 ± 45	333 ± 70	1352 ± 39
1.621 – 1.660	733 ± 106	392 ± 61	527 ± 61	909 ± 47	168 ± 72	1322 ± 40

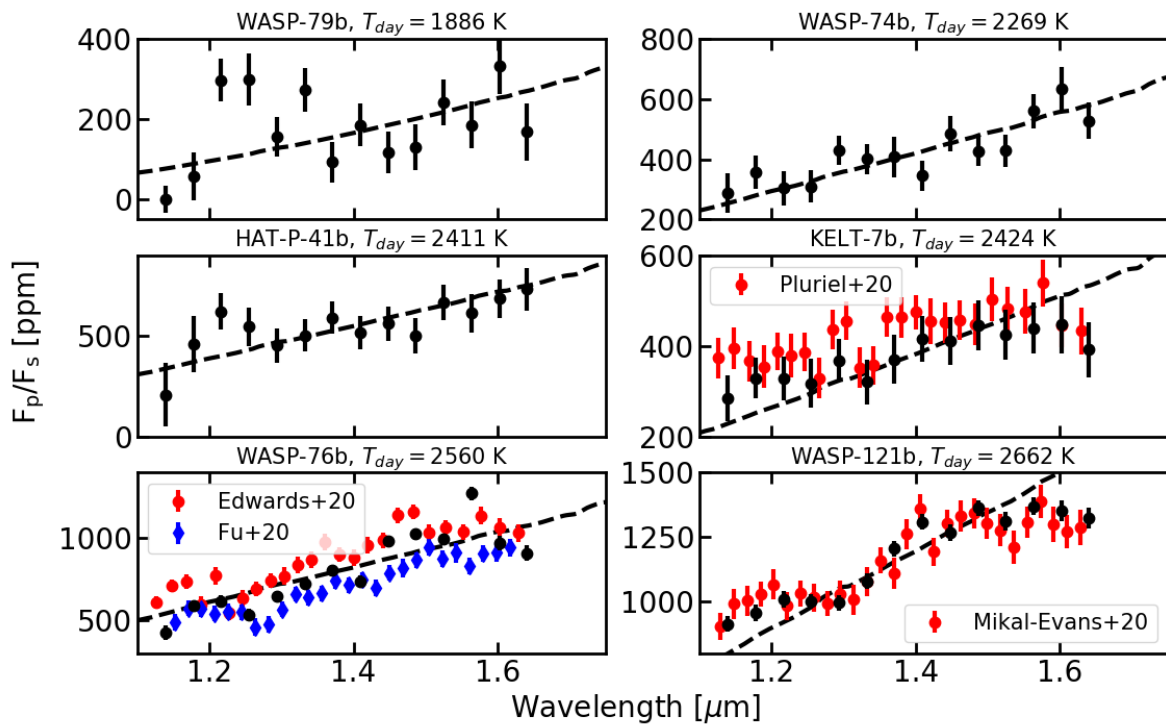
Supplementary Table 4. Secondary eclipse spectra for the six planets for which new data reductions were performed in this work. All eclipse depths are in units of ppm.



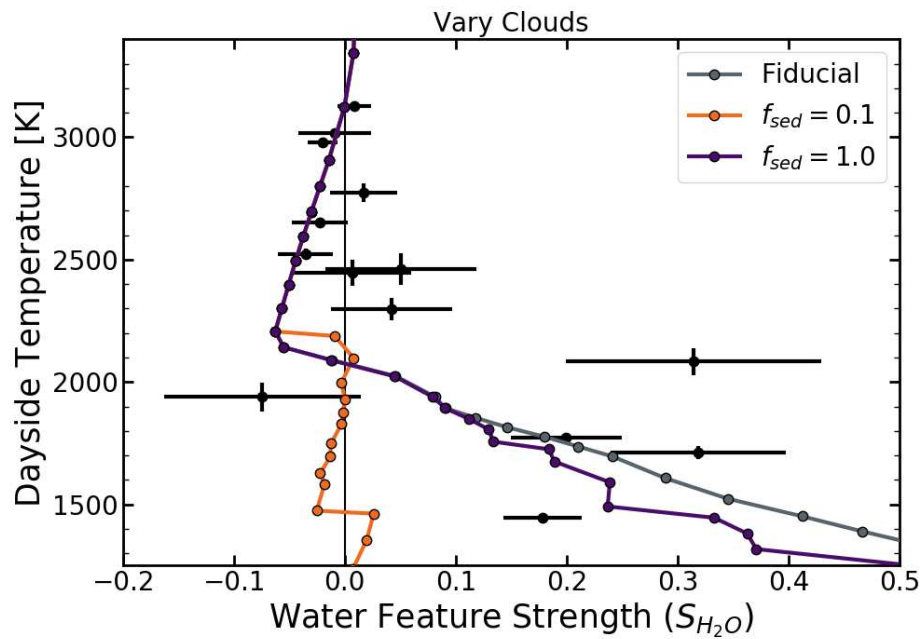
Supplementary Figure 1. Construction of the *HST* water feature strength metric to compare observed spectra to models. Blue points show *HST*/WFC3 observations of WASP-43b⁵. The orange and green shaded regions indicate the spectral extent of the “out-of-band” and “in-band” flux, which are defined based on where the models in Figure 2 show water features. The gray line with circular points shows the best-fit model interpolated from those in Figure 2. The gray line with diamond-shaped points shows a blackbody fit to the out-of-band flux region.



Supplementary Figure 2. Same as Figure 1, but with shaded bands indicating the “out-of-band” and “in-band” regions used to calculate the water feature strength (S_{H_2O}) for each observed secondary eclipse spectrum.



Supplementary Figure 3. *HST*/WFC3 secondary eclipse spectra for the six data reductions presented in this paper (black points). Black dashed lines indicate best-fit blackbody spectra, and temperatures above each plot give the corresponding dayside temperature T_{day} . Red points show previous data reductions from the literature^{6,31–33}, which all show good agreement with the results presented here.



Supplementary Figure 4. Change in *HST* water feature strength when clouds are added to the fiducial model. The grey line shows the fiducial model, while the orange and purple lines show cloudy models with sedimentation efficiencies of $f_{sed} = 0.1$ and 1.0 , respectively. Adding clouds to the model effectively weakens the water feature strengths and makes the emission spectra more blackbody-like below dayside temperatures of about 2000 K. However, clouds have no effect on S_{H_2O} at $T_{day} \geq 2000$ K because the planets' daysides are too hot for any condensation to occur.

Figures

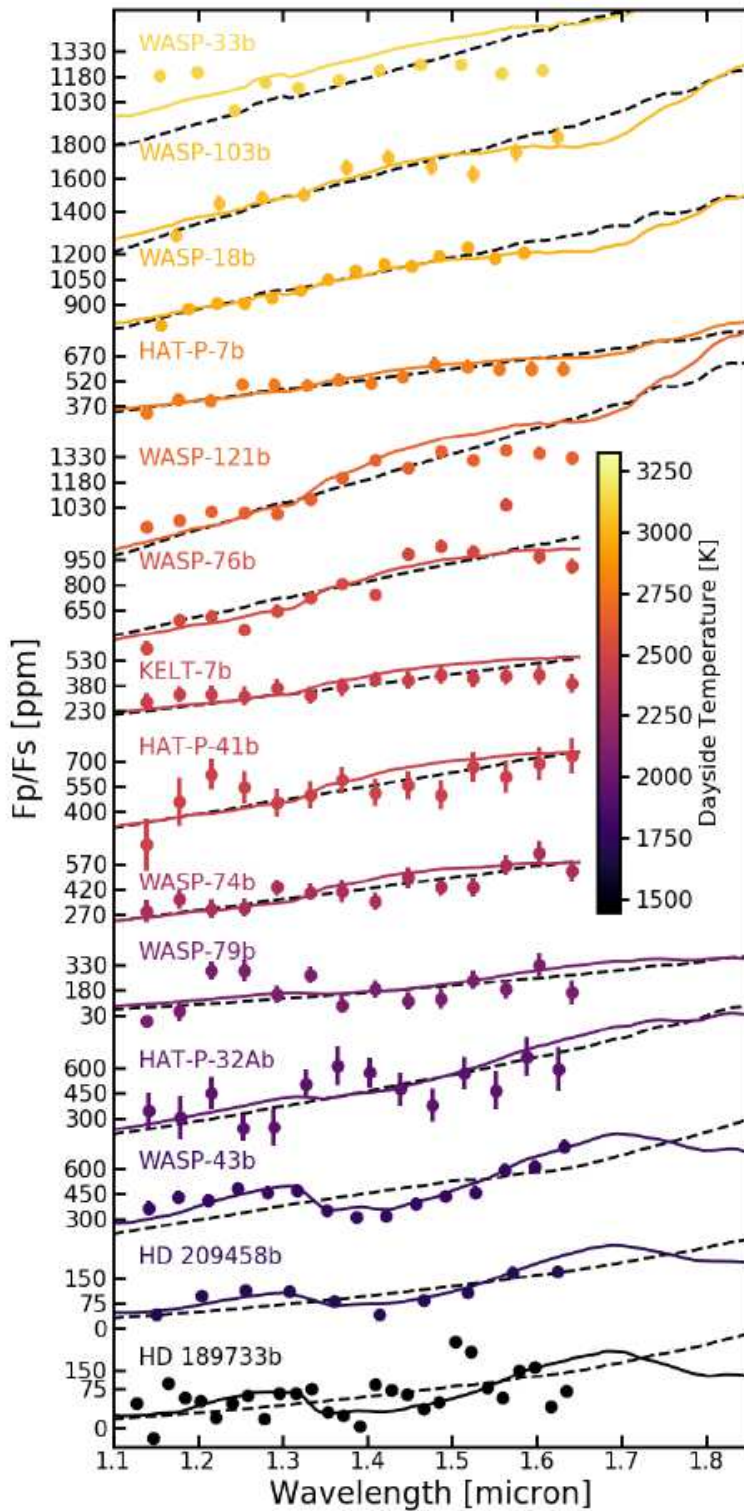


Figure 1

Secondary eclipse spectra for all 14 hot Jupiters considered in this study. Data sets are colored by dayside temperature, which is measured as described in the Methods and shown by the colorbar. Solid lines indicate interpolations from our solar composition fiducial model grid (see the Methods section for a

description), while dashed lines indicate best-fit blackbodies. Note that for several data sets, the error bars are smaller than the point size.

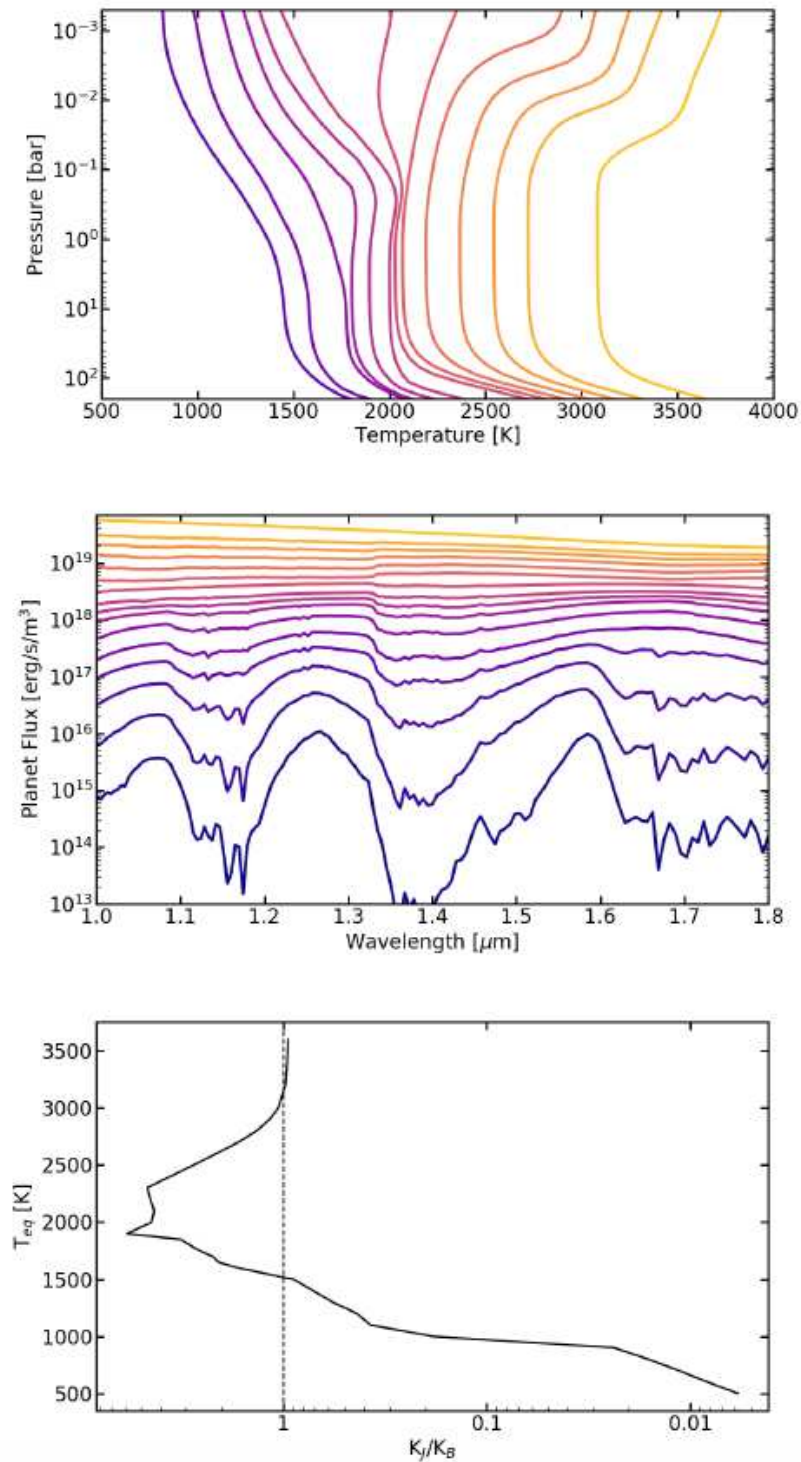


Figure 2

Temperature-pressure (T-P) profiles (top) and resulting dayside planet fluxes (middle) for the fiducial model grid, which covers approximately the same range of temperatures as spanned by the observations. The full model specifications are detailed in the Methods. The fiducial model uses a 5300 K stellar

effective temperature, a solar composition planetary atmosphere ($[M/H] = 0.0$ and $C/O = 0.55$), a planetary gravity of 10 m/s^2 , and a planet internal temperature of 150 K . Blue and yellow lines show models with the coolest and warmest irradiation temperatures, respectively. For clarity, only every other model in the grid is shown here. The bottom panel shows the ratio of the absorption mean opacity (k_J) to the Planck mean opacity (k_B) as a function of equilibrium temperature in these models at a pressure of 10^{-2} bar . This ratio describes the relative efficiency of heating vs. cooling in the models, and a ratio of $k_J/k_B > 1$ generally indicates the presence of a thermal inversion in the temperature-pressure profile. This panel is plotted with temperature on the y-axis for ease of comparison to Figure 3.

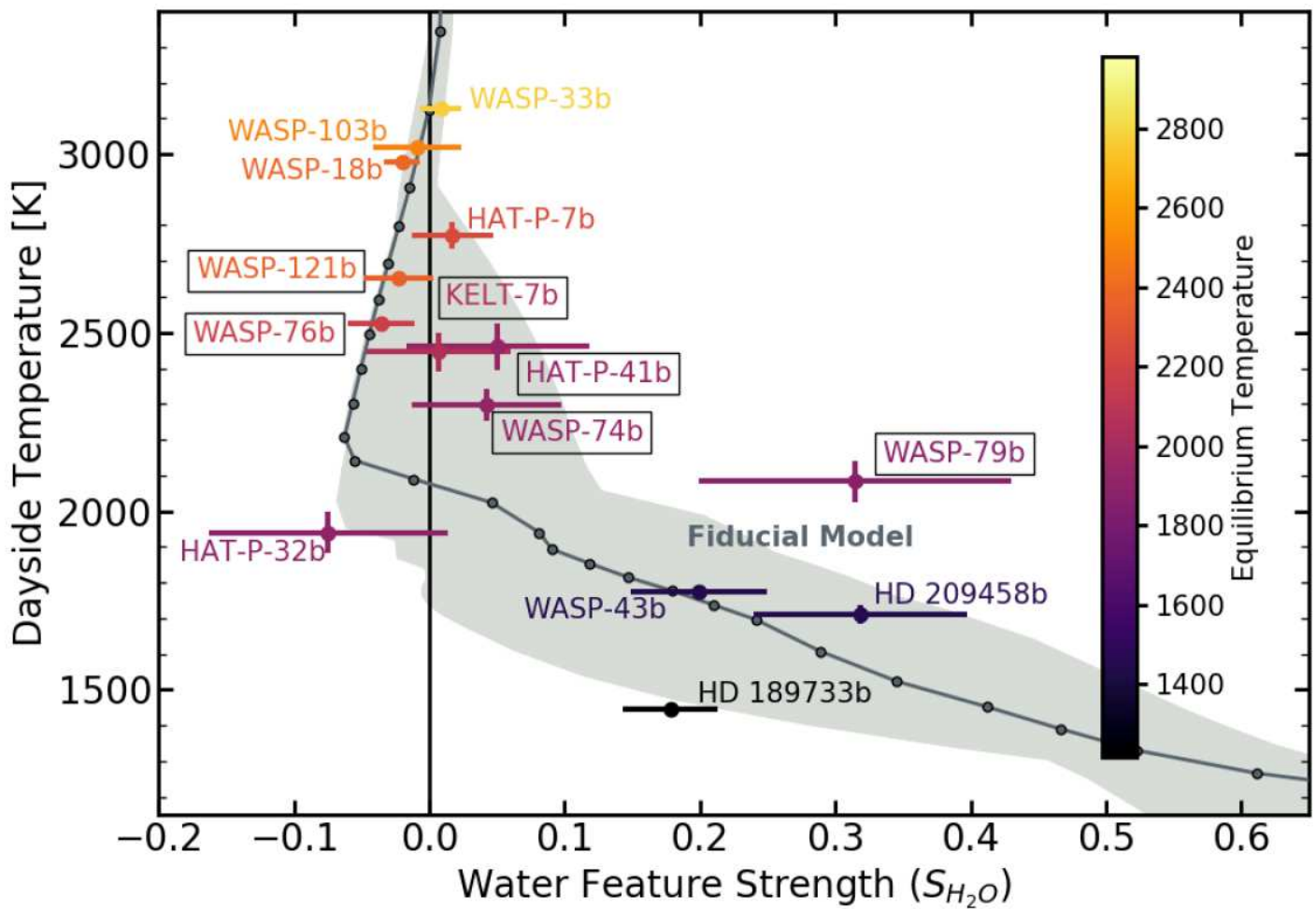


Figure 3

HST water feature strength diagram comparing observed secondary eclipse spectra to the model predictions in Figure 2. The y-axis shows the temperature of a blackbody fit to the “out-of-band” regions defined in Supplementary Figure 1, which is the observed dayside temperature T_{day} . The x-axis shows the strength of the observed feature in the water band at $1.4 \mu\text{m}$ compared to this blackbody, as defined by Equation 1. Featureless, blackbody-like spectra have $S_{H_2O} = 0$ and absorption/emission features have positive/negative colors, respectively. The gray line and points show the fiducial models pictured in Figure 2. The light gray shaded region shows the full range of model predictions assuming different values for the stellar effective temperature; the temperature where TiO opacity becomes important; and the planet

gravity, C/O ratio, metallicity, and internal heat. Colored points with error bars show all planets with HST/WFC3 spectra observed in the spatial scanning mode, and boxes around planet names indicate new data reductions in this publication. The color scale indicates the planetary equilibrium temperature. The error bars include uncertainties in the stellar effective temperature.

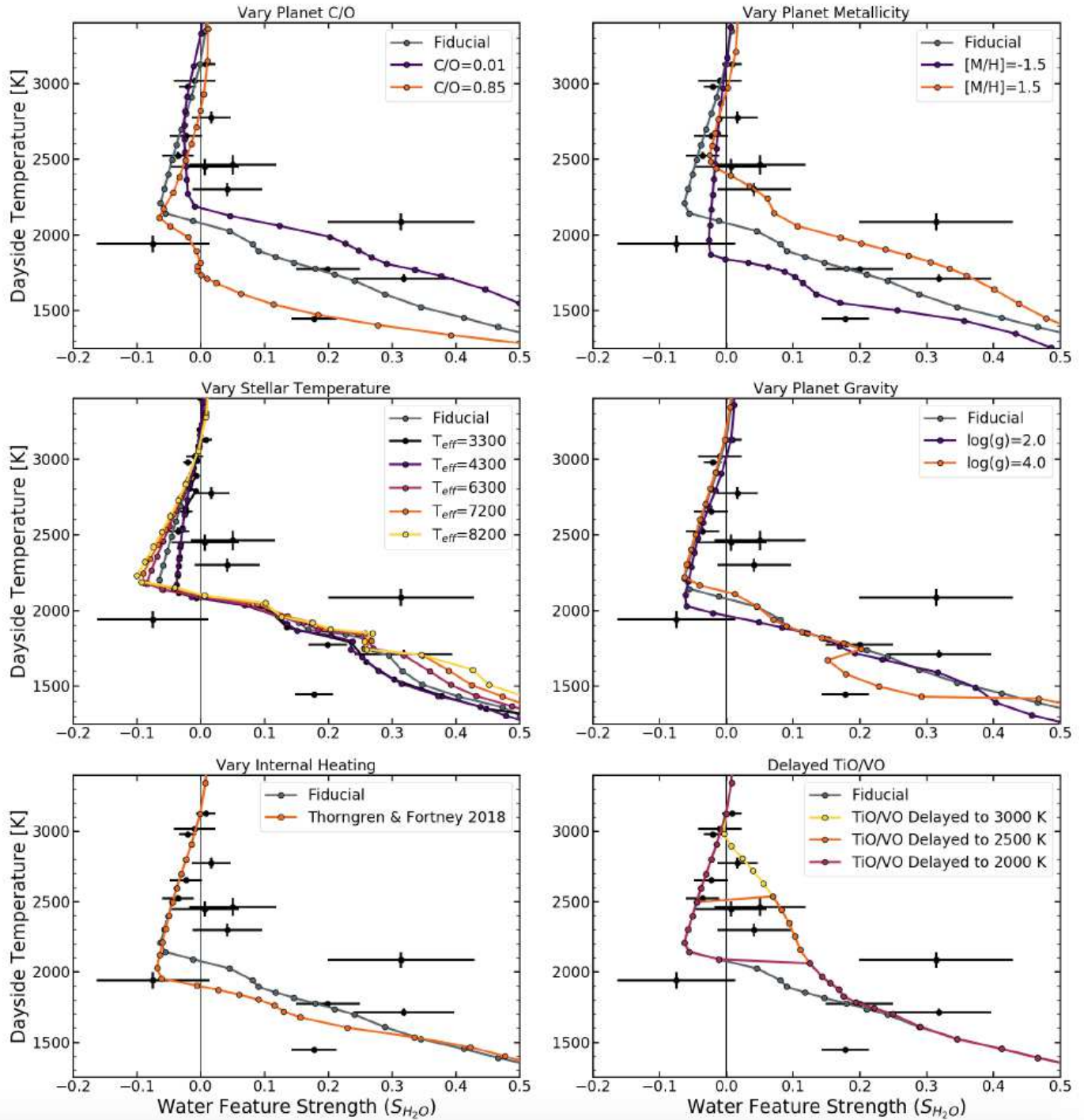


Figure 4

Diagrams illustrating the change in HST water feature strength from models with different parameters. All diagrams show the observed data as black points with error bars, while the lines show tracks for models with varying C/O ratio (top left), metallicity (top right), stellar temperature (middle left), gravity

(middle right), internal heating (bottom left), and the temperature to which TiO opacity was ignored (bottom right). In each case all other parameters are held fixed at the fiducial model values. The error bars include uncertainties in the stellar effective temperature. We found that changing the stellar temperature, planetary gravity, and internal heating in our models had little impact on the derived water feature strengths, and changing the TiO/VO only had an impact at intermediate temperatures, but changing the atmospheric C/O ratio and metallicity can explain the diversity of observed secondary eclipse spectra.